



**HAL**  
open science

# Designing a Contact Fingertip Sensor Made Using a Soft 3D Printing Technique

Alejandro Ibarra, Baptiste Darbois-Textier, Francisco Melo

► **To cite this version:**

Alejandro Ibarra, Baptiste Darbois-Textier, Francisco Melo. Designing a Contact Fingertip Sensor Made Using a Soft 3D Printing Technique. *Soft Robotics*, 2022, 10.1089/soro.2021.0128. hal-03621780

**HAL Id: hal-03621780**

**<https://hal.science/hal-03621780>**

Submitted on 28 Mar 2022

**HAL** is a multi-disciplinary open access archive for the deposit and dissemination of scientific research documents, whether they are published or not. The documents may come from teaching and research institutions in France or abroad, or from public or private research centers.

L'archive ouverte pluridisciplinaire **HAL**, est destinée au dépôt et à la diffusion de documents scientifiques de niveau recherche, publiés ou non, émanant des établissements d'enseignement et de recherche français ou étrangers, des laboratoires publics ou privés.

# Designing a contact fingertip sensor made using a soft 3D printing technique

Alejandro Ibarra, Baptiste Darbois Texier and Francisco Melo \*

## Abstract

The development of highly compliant materials and actuators has enabled the design of soft robots that can be applied in rescue operations, in secure human-robot interactions, to manipulate fragile devices or objects, and for robot locomotion within complex environments. In order to develop reliable solutions for soft robotics applications, devices with the ability to deform and change shape are required, which must be equipped with appropriate sensors capable of withstanding large deformations at suitable speeds and respond repeatedly. This work presents a methodology to build strain sensors made of sensitive, thin and conductive channels printed inside a soft matrix, using 3D printing. As proof of concept, rectangular beams and semi-spherical caps embedded with sensitive circuits are developed, that are designed to deform under applied forces and detect the gradual contact with objects. The rectangular beam with conductive lines separated from the neutral plane exhibits a quasi-linear electrical response as a function of the applied shear strain. Mechanical diodes, which trigger an activated response once a given deformation onset is exceeded, are implemented using circumferential conductive-channels that are centered with the spherical body sensor. Sinusoidally shaped conductive channels located at a given distance from the spherical surface produce a monotonic electrical response, which detects deformations over a broad range. Linear sensors, with enhanced sensitivity to compression, are created if the sensitive conductive channels are oriented along the compression direction. Numerical calculations, used to guide the design of the sensor, show the capability of these sensors to measure simultaneous normal and tangential forces, making them suitable for applications involving fragile object manipulation and robot locomotion. An example of application of these sensors in the control of the forces applied by soft gripper lifting an object is given.

**Keywords:** Soft robotics, Soft sensors, Deformation gauges

## 1. Introduction

Human fingertips sense information that is processed to coordinate sequences of muscle motion, used to manipulate objects and perform haptic actions. The somatosensory system relies on a wide variety of mechanoreceptors to sense the complex interactions taking place on our skin's surface. It is possible to identify and discriminate between vibrations, object size and texture, changes in shape, pressure and even pain with a

high degree of sensitivity and resolution.<sup>1</sup> In addition to sense, strategies to transmit information to the central neural system and the subsequent analysis of this information are crucial stages in an efficient somatosensory system. For soft robotic applications, mechanical transducers or sensors must be designed within a soft artificial body and act in sync with soft actuators. These sensors can be manufactured following a variety of working principles, most commonly these use resistive<sup>2</sup>

---

\*Alejandro Ibarra and Francisco Melo are members of the Physics Department and The Center for Soft Matter Research, Smat-C, of University of Santiago, Avenida Ecuador 3493, Estacion Central, Santiago-Chile. [alejandra.ibarra@usach.cl](mailto:alejandra.ibarra@usach.cl), [francisco.melo@usach.cl](mailto:francisco.melo@usach.cl). Baptiste Darbois Texier is member of Universite Paris-Saclay, CNRS, FAST, 91405, Orsay, France. [baptiste.darbois-texier@universite-paris-saclay.fr](mailto:baptiste.darbois-texier@universite-paris-saclay.fr)

or capacitive<sup>3</sup> sensing technology, however other novel techniques may be used, such as, Electrical Impedance Tomography (EIT)<sup>4</sup> and soft light guides.<sup>5</sup> Both latter techniques require a knowledge of the local impedance change as well as detecting the light deflection caused by the reversible deformation of the soft body sensor, respectively. These sensors are manufactured using several layers of thin structured sheets deposited sequentially<sup>2</sup> resulting in a variety of devices suitable for many applications. For instance, a novel 2D printing technique based on direct ink writing with eutectic gallium-indium (EGaIn) was used to fabricate a sensing glove that replicates finger motion.<sup>6</sup> Similarly, soft resistive sensors, used to detect positions and reconstruct objects forms, have been developed using 2D printing to produce conductive circuits made of a mix of inexpensive carbon black with an uncured silicone elastomer, which enables conductivity at high stretch.<sup>7</sup> Despite these important advances in techniques, applications often require an understanding of deformation within an entire three-dimensional structure, and not only near to the structure's surface. For example, sensors capable of the simultaneous identification of both normal and shear forces are essential in the development of soft fingertips suitable for the manipulation of fragile objects. In addition, these sensors require sufficient spatial resolution and frequency response to ensure a satisfactory feedback control. Novel techniques for the 3-D printing of soft gels<sup>8</sup> provide a foundation for the development of three-axial sensors embedded in a soft matrix, without being geometrically restricting to a two-dimensional plane. As recently demonstrated,<sup>9</sup> 3-D printing techniques come along with the capability of manufacturing force arrays sensors based on deformable deflectors which are designed to modulate the outgoing signal light according to the applied force. Thus, soft arrays can benefit from fiber optics and charge coupled devices technology to offer spatially resolved sensors.

In this article, a versatile 3D-printing technique is developed to build a fingertip sensor, composed of conductive and deformable circuits immersed in a rectangular or semi-spherical soft matrix. Furthermore, it is demonstrated that the electrical resistance response of the sensor can be

designed to optimally react to deformations resulting from normal and shear forces. This work aims to recreate the sensitivity of the human sense of touch, which can be used in applications such as the handling of fragile objects and to design devices and sensors that aid in the prevention of injuries in sports and biomechanics. If a spherical shape is pressed against relatively flat or rounded surfaces, it deforms following a nonlinear force response, as dictated by Hertz's potential.<sup>10</sup> The advantage of this response is that soft spherical caps can more easily adapt to the shape of an object during handling, and they display a compressive stiffness that increases progressively with deformation. This study focuses on two types of soft silicone contact sensors: rectangular beams and hemispherical caps. The beam sensor embeds conductive lines that are separated from the neutral plane in order to confer a high sensitivity to lateral deflections. For the hemispherical geometry, three sensors were built with the following variations; First, a simple sensor with a sensitive circuit, in the form of an inner semi-circumference (centered with the main body) and a circular section with a diameter that measures a fraction of a millimeter. This sensor shows a highly non-linear response, similar to a mechanical diode, which activates at a threshold that depends on the distance of the sensitive component from the sensor surface. Based on this result, a second modified sensor was built using a sensitive resistive circuit of sinusoidal form. This solution enhances the net deformation of the sensitive circuit under external compression, leading to a more sensitive and monotonic response, more appropriate for linear detection. A third configuration was developed to explore a combination of semi-circumferential sensors, by positioning two sensitive semi-circumferential circuits at different depths. This aims to provide a highly sensitive sensor, capable of triggering alerts when critical loads are exceeded. Simple numerical calculations using finite elements strategy alongside hyperelastic models are used to guide the sensor design. Finally, based on this methodology of modeling, the theoretical response of more sensitive and linear contact sensors is calculated. For example, it is demonstrated that linear sensors with enhanced sensitivity are achieved when the sensitive

conductive circuit is oriented along the compression direction. To conclude, this study presents a hemispherical sensor, consisting of two symmetric conductive circuits, located in opposite quadrants, to detect simultaneously the compression and shear stress. An example of application with a gripper handling an object is given.

## 2. Materials and Methods

### 2.1. Soft sensors manufacturing

For the manufacture of soft sensors, we use a 3D printing technique that permits to produce soft conducting circuits of desired shape embedded in a soft matrix.<sup>11</sup> This 3D printing technique is based on direct ink writing and was adapted from the description by Abigail.<sup>8</sup> It consists in injecting a conductive fluid into a viscoplastic matrix within a mold that imposes the exterior form of the matrix [Fig. 1a]. The injection is achieved through a nozzle and a syringe pump, which controls the volume of the material being added. In a previous study,<sup>12</sup> injection control was achieved by monitoring the pump pressure, which permitted rapid changes in the injector flow but also caused a loss of control of the volume of ink being injected. In order to accurately control the injected volume, the efficiency of the process was optimized, and the injection system was purged prior to printing in order to eliminate excessive gas volume. The injection is carried out through a syringe pump, and a 1mL syringe and a 24 gauge nozzle allowed to obtain conductive channels of suitable dimensions. The 3D printer is configured with a standard Cartesian configuration. To conserve volume, the diameter of the trace is controlled with the nozzle movement. Indeed, to print a line with a length  $\ell$  (the distance travelled by the nozzle) and diameter  $D$ , with a syringe of diameter  $D_s$ , the syringe's plunger moves a distance  $L$ . The material being injected is incompressible, thus the volume injected is the same as that displaced by the syringe  $\pi(D_s/2)^2L = \pi(D/2)^2\ell$ , which for given  $\ell$  and a desired  $D$ , leads to  $L = \ell(D/D_s)^2$ .

[Figure 1 about here.]

The matrix is made of the commercial silicone Ecoflex™ 00-50 (Smooth-On), with parts A and B mixed in a 1:1 ratio. Cure time is increased

through the addition of Slo-jo™ (Smooth-On) (1.2 %w/w with respect to part B) and Thivex (Smooth-On) thixotropic agent (0.5 %w/w with respect to part B). This procedure allows to reach working times of 20 min at room temperature ( $T = 20^\circ\text{C}$ ). To prevent bubble formation after mixing, the silicone is degassed and then poured into the mold. Molds are designed to allow continued degassing of the mixture, which leads to more homogeneous matrix. The molds were built using a 3D FDM (Fusion Deposition Modeling) printer, using commercial PLA (Polylactic Acid), with a vertical resolution of  $50\mu\text{m}$ . To minimize roughness, caused by this printing technique, molds were sanded by hand to improve the finishing of the sensor's surface. The conductive channel is made by injecting<sup>11</sup> a suspension of Aerosil 200 (Fumed Silica) to 6%w/w in EMIM-ES (1-Ethyl-3-methylimidazolium ethyl sulfate  $\geq 95\%$  from Sigma-Aldrich). After mixing, the suspension is degassed and loaded into a syringe. After printing, the typical curing time of the matrix is about 1 hour at  $T = 20^\circ\text{C}$ , and 30 min at  $T = 50^\circ\text{C}$ .

In order to characterize the channels, a removable ink, made from a Pluronic F127 (Sigma-Aldrich) suspension in deionized water, is used to determine the dimensions of the channels produced by this printing technique. This suspension is a gel at room temperature and becomes fluid below the gelling temperature ( $4^\circ\text{C}$ ). Thus, the ink can be removed from the channels once it is cooled. The channels are characterized using the following steps: i) we manufacture a rectangular mold of dimensions 50 mm by 25 mm, and 5 mm deep, and the silicone is poured into this mold. ii) we use removable ink to print seven lines of 20 mm length for different extrusion diameters. The prints were repeated four times at each printing speed. iii) After curing, the silicone is cut into three sections (transverse to the printed lines) and is cooled to remove the ink. The cross section, determined by image analysis, indicates that the channel diameter is not impacted by the printing speed [Fig. 1b]. However, the experimental points reveal a sub extrusion with compared to the expected value (the red line in [Fig. 1b]).

## 2.2. Soft sensors design

To establish a proof of principle, two types of sensors were built. The first type is designed to measure large deflections and consists of a rectangular beam that embeds conductive lines [Fig. 2a]. These lines are separated from the neutral plane in order to obtain enough sensitivity. This setup is similar to the description in Tapia Knoop Mutný et al.,<sup>13</sup> which focuses on an automated sensor design for proprioceptive soft robots. The second type of sensors is designed to detect soft contacts and are built within a semi-spherical soft cap, with sensing lines positioned at a fixed distance from the curved surface. We implement three different geometries of circuits: (i) an inner semi-circumference (centered with the spherical body) with a 13 mm radius and a circular section measuring 510  $\mu\text{m}$  diameter [Fig. 3b], (ii) a sensitive resistive circuit in a sinusoidal form [Fig. 3c] and (iii) two sensitive semi-circumferential circuits at different depths [Fig. 3d].

## 2.3. Soft sensors characterization

The electrical response of the embedded circuit to a mechanical deformation is characterized using a voltage divider with a 1 M $\Omega$  reference resistor and a Teensy 3.2 development board to determine the voltage. The typical resistance per unit of length of the sensitive channels is 9.56 k $\Omega$ /mm for a 0.5 mm diameter channel. Electrical connections are made using gold coated pins introduced at the free end of the conductive channels, which provides good repeatability of the electrical measurements.

In order to impose a deformation to the beam sensor, the tip is submitted to a local force that induces a lateral deflection. Markers were painted on the sensor surface to observe its deflection. In the case of hemispheric sensors, the mechanical deformation is imposed by a 8 mm diameter acrylic cylinder with a rounded tip [Fig. 3a] that is indented into the soft sphere up to a maximum of 5 mm depth, at a constant speed of 0.5 mm/s. The normal force applied by the cylinder is measured using a load cell, Futek LBS200 S-Beam, operating within  $\pm 2$  N.

The dynamic response of the sensor is tested by imposing sinusoidal vibrations of small ampli-

tudes to the indenter by the way of an electromechanical vibrator. The amplitude is defined using an accelerometer signal coupled to the indenter body. We evaluate the resistance change at different indentation depths, over a range of driving frequencies, as a function of the acceleration peak.

## 2.4. Soft sensors modelisation

To further understand the sensor response, a mathematical model is used to determine the resulting strain distribution along the sensitive elements and its consequence on the resistive element. We use finite element numerical simulations (FEM) through the Comsol package where the elastic body is modeled as a hyper-elastic solid of shear modulus  $\mu$  and compressibility modulus  $\kappa_0$ . The mechanical deformation of the sensor is accounted by a rigid object that indents the sensor at depth,  $d$ . We first calculate the deformation field of the soft body without considering the sensitive element and then assume that the presence of any thin channel inside the body sensor will follow the deformation experienced by a continuous body. This calculation is expected to be valid for a sufficiently thin sensitive element i.e. when there is a large overall variation in the strain field compared to the sensitive channel diameter. Then, the resistance is modeled as a thin wire that follows the curve  $s$ , which is described by the position vector  $\mathbf{p}(s)$ , and a tangent vector,  $\hat{t} = \mathbf{p}'(s)/|\mathbf{p}'(s)|$ . The curve is discretized in  $N = 100$  segments, of length  $l_i$ , cross section  $A_i$ , and with a material resistivity of,  $\rho$ . Therefore, the resistance,  $r_i$ , of such an element is written,

$$r_i = \rho \frac{l_i}{A_i} \quad (1)$$

The changes in  $l_i$  and  $A_i$  are calculated from the simulations. Variations in length can be computed as  $l_i = \lambda_t l_{i0}$ , where  $\lambda_t$  is the stretch along the  $\hat{t}_i$  direction and is calculated as  $\lambda_t = \sqrt{\hat{t} \cdot \mathbf{C} \cdot \hat{t}}$ , where  $\mathbf{C} = \mathbf{F}^T \mathbf{F}$  corresponds to Green's deformation tensor. The volume of each cylindrical resistor is  $V_i = J V_{i0}$  where  $V_{i0}$  is the volume with no deformation, and  $J$  corresponds to the invariant  $J = \det(\mathbf{F})$ , ( $\mathbf{F}$  is the deformation gradient tensor). To calculate changes in the cross section  $A_i$ ,

$V_i = l_i A_i$  is considered, therefore  $A_i = JA_{i0}/\lambda_t$ . The total resistance of the sensitive element is the sum over  $i$ ,  $\sum r_i$ . In order to prepare a model of the system, the relative resistance change is used, i.e, the changes in resistance as a result of conductivity variations of EMIM-ES, due to moisture absorbed from the environment, is also accounted for. Finally, the relative resistance change expresses as

$$\frac{\Delta R}{R_0} = \frac{1}{R_0} \sum^N \frac{l_{i0} \lambda_t^2}{JA_{i0}} - 1 \quad (2)$$

### 3. Results

#### 3.1. Beam sensor

The electrical resistance of the beam sensor [Fig. 2a] is measured at the point of several deflections. Figure 2b presents a superposition of the beam for increasing deformations. The relative change of circuit resistance is observed to increase quasi-linearly with shear strain [Fig. 2c]. In parallel, finite element simulations (FEM) are used to predict the strain field of the deformed structure. In order to validate this description of beam deformation, the subsequent changes in resistance are calculated following the geometrical changes of the conductive channel, and compared with the measured values as a function of the beam deflection, [Fig. 2c]. Generally, the main features of channel resistance with deflection are observed using numerical values, however for large beam deflections, the simulations deviate from the measured values. The relative resistance change along the sensitive element is calculated using the incompressible and compressible models, which correspond to setting  $J = 1$  (green line) and  $J > 1$  (red line) respectively, [Fig. 2c]. Observations indicate that the compressible model gives a better reconstruction of the experimental results in the low bending regime, however it tends to overestimate changes in resistance for large bending amplitudes. This is because this theoretical approach does not consider the actual boundary conditions at the boundaries of the conductive channel. In this case, conductive gel may

leak from the end of the channel, causing a decrease in channel resistance with respect to the incompressible model.

[Figure 2 about here.]

#### 3.2. Hemispherical sensors

The electrical responses of the three designs of hemispherical sensors to indentation are presented in Fig. 4 with dots. The semi-circumference sensor displays a non-monotonic response with an initial decrease which then abruptly increases [blue dots in Fig. 4b]. This response is reminiscent of a diode where there is a rapid increase in resistance after displacement. The sinusoid sensor exhibits a stronger response with a monotonic trend [red dots in Fig. 4b]. Thus, the sinusoidal form is proved to enhance the net deformation of the sensitive circuit under external compression and improve the overall sensitivity. The third configuration (two sensitive semi-circumferential circuits at different depths) shows a non-monotonic response but with distinct deformation onsets [dots in Fig. 4c]. This critical displacement depends on the location of the sensitive part with respect to the free surface of the sensor. For the  $R_1$  sensor this is about 1.4 mm, whereas for the  $R_2$  sensor it is about 2.8 mm. This diode-like response can be useful for applications requiring to limit the prehension force in order to avoid object damage.

[Figure 3 about here.]

Thereafter, we want to compare our measurements with the predictions of the FEM simulations. The first step is to confirm that the simulation correctly accounts for the indentation experiment. The force measured during assays is first compared with the reaction force on the indenter [Fig. 4a]. The hyperelastic parameters of the simulations are adjusted to better fit the experimental force experienced by the indenter. The optimal parameters found for an nearly incompressible neo-Hookean model are  $\mu = 0.074$  MPa and  $\kappa_0 = 0.1653$  MPa, which are similar to previously reported values.<sup>14</sup>

[Figure 4 about here.]

These parameters are used to compute the response of the three semi-spherical sensors depicted in Figs. 3(b-d). These predictions are plotted in Figs. 4(b-c) by the way of solid lines. Whatever the sensor design, the numerical approach is only able to capture the electrical response at sufficiently small indentations. This discrepancy may arise from the fact that our approach neglects the collapse of the channel at large indentations.

To understand the non-monotonic behavior of the circumferential sensor, the resistance variation as a function of angular coordinate,  $\theta$  [defined in Fig. 3b], is explored with respect to the indenter axis using the numerical approach. Simulations reveal that in the central zone, there is a relative increase in resistance [Fig. 5] as the sensitive part of the sensor is subjected to traction. On the contrary, the relative resistance decreases in the external zones due to compression. Thus, at low indentation levels, compression dominates in the external zone, while the contrary is true at high levels of indentation. Finally, it is possible to analyze the width of the central zone by measuring the angular aperture,  $2\phi$  between the two observed maxima in Fig. 5. From this angle, the size of the traction zone,  $a$ , can be defined as,  $a = R_s \sin \phi$ . The inset in Fig. 5 shows that  $a \approx \sqrt{bd}$ , with  $b \approx 1.66$  mm, indicating that the size of the traction zone follows a simple geometric constrain.

[Figure 5 about here.]

### 3.3. Design strategies for a linear sensor

To develop strategies for sensor design, this section explores distinct orientations of the sensitive circuit inside the semi-spherical sensor. Previous sections observe an increase in circuit resistance below the indenter when the sensitive resistive circuit follows the cylindrical geometry, whereas circuit resistance decreases outside this area. This effect results in a mechanical diode type behavior. Thus, changes in electrical resistance are linked to local deformation in the sensitive circuit: compression along the sensitive channel causes a decrease in resistance while traction in the same direction leads to an increase in resistance. Thus, monotonic behavior is predicted when the sensitive channels are oriented along trajectories experiencing only one type of mechani-

cal deformation. Figure 6 illustrates two design examples, both presenting an almost linear response to indentation. A triangular shape, with an aperture angle that varies with respect to the indentation axis [Inset Fig. 6a], indicates that maximum sensitivity occurs when the sensitive element is just below the indenter and parallel to the indenting axis [Fig. 6a]. In addition, a wider range of sensor linearity is obtained for smaller triangle base. A comparison is made with a rectangular sensitive element that is parallel to the indenter axis [inset in Fig. 6b] which reveals an increase in sensitivity with the height of the sensitive circuit [Fig. 6b].

[Figure 6 about here.]

### 3.4. Dynamical Response

[Figure 7 about here.]

For practical applications, it is necessary to evaluate the dynamical response of the soft sensor to ensure that it does not become too small at high excitation frequencies due to the relatively low elastic constant value of the soft matrix. The response of the sensor, evaluated by its resistance variation  $\delta R$ , maintaining a constant acceleration peak and a given static indentation,  $d_s$ , decreases with increasing driving frequency. However, it is better to determine the sensor's frequency response through sensitivity variations within the resistive element, with small amplitude variations during indentation, defined as  $\partial R/\partial d$ . This indicates the change in the sensor's resistance induced by a change in the indentation amplitude at a given frequency and a given static indentation  $d$ . It is observed that  $\partial R/\partial d$  is a weak function of frequency [Fig. 7] but increases with static indentation. Thus, it is proved that soft sensors can be fabricated with sensitivities in the order of 1 k $\Omega$ /mm, over a relatively broad range of frequencies. In terms of force and relative resistance changes throughout the circuit, sensitivities in the order of several percent per Newton can be easily achieved.

### 3.5. Sensing tangential force

A challenge within manipulating systems is how to apply enough forces on an object to gener-

ate a sufficient friction and handle it without damage. Therefore, sensors that include both normal and tangential forces are an essential step in the development of devices suitable for the manipulation of fragile objects. Using the workflow presented previously, it is possible to design a semi-spherical soft sensor composed of conductive elements, sensitive to normal and tangential forces. First, to characterize the response of the displacement field of the matrix, a numerical simulation protocol is carried out, where the semi-spherical soft body is initially pressed in a normal direction using a rigid flat object. Subsequently, it is tangentially displaced until sliding occurs. For applications, typical values of the indentation depth, the tangential displacement and the friction coefficient are:  $\tilde{u}_z = 2.5$  mm,  $\tilde{u}_y = 2.5$  mm and  $\mu = 0.2$  respectively.

[Figure 8 about here.]

The effect due to normal force, tangential force and the sliding of the flat indenting object on the displacement fields are visualized through the numerical simulation [Fig. 8a]. Tangential force breaks the mirror symmetry of the strain field, favoring either compression or dilation at the opposite quadrant on the matrix. The behavior at each stage can also be seen in the force graph [Fig. 8b], where the vertical force  $F_z$  increases with normal displacement, but remains constant in the shearing and slipping stage. The tangential force,  $F_y$ , is zero in the indentation stage, and increases monotonically with increasing tangential displacement and reaches a constant value in the sliding stage. It is observed that in this latter stage, the tangential force equals the frictional force,  $F_y = \mu F_z$ .

[Figure 9 about here.]

Subsequently, sensitive elements of tangential forces are envisioned using two conductive filaments in semi-arches, joined at the top, and separated by a distance of 4 mm at the base of the semi-spherical matrix [Fig. 8c]. This structure is oriented in the direction of the horizontal movement and the response of the sensor is evaluated in both directions of movement. The sensor has a linear response to compression. In the shear stage, the response is also linear to displacement, but it is more sensitive [Fig. 8d]. In the sliding stage

shear response is constant and determined by the maximal friction sustained by the sliding object, which is consistent with frictional laws.

In order to distinguish the shear signal from the compression signal, an additional symmetric circuit, located in the opposite quadrant, is added [Fig. 9a]. Thus, defining the reading of circuits in the positive and negative quadrants as  $R_+$  and  $R_-$  respectively, and by using the inversion symmetry obeyed by the contributions of the shear forces to the readings,  $S_+$  and  $S_-$ ,  $S_+ = -S_-$ , the compression and the shear forces,  $C$  and  $S$  respectively, write,  $C = (R_+ + R_-)/2$  and,  $S = (R_+ - R_-)/2$ . Sensitive quadrants are oriented to sense shear along the horizontal axis. Figure 9b illustrates the sequence defined to test the sensor functioning (See Movie 1, in Supplemental Information, showing the whole cycle): i) The compression stage: finger is pushed parallel to the main axis of the sensor (normal movement). The variations of both  $R_+$  and  $R_-$  have the same sign [Fig. 9c]. ii) the finger is pushed along horizontal axis (positive shear); readings  $R_+$  and  $R_-$  have opposite signs as expected [9c]. iii) Shear inversion (negative shear). iv) Compression is released. Finally, the compression  $C$  and the shear  $S$ , are obtained, for every step of the testing cycle [Fig. 9c]. The results of this test prove that this design is adapted for applications requiring to detect a shear motion. With this objective in mind, we implement a gripper in which one tip consists of the previous sensor and allows to detect the shear associated to the prehension of an object [Fig. 9d] (See also Supplemental Information, Movie 2).

#### 4. Conclusion

This 3D printing methodology is able to print a resistive channel immersed within a soft body and has facilitated the manufacture of prototype semi-spherical soft sensors, which are able to respond to both linear and non-linear compression. The preparation methodology of the soft spherical matrix requires minimal molding, and the sensitive elements can be installed simultaneously in a single step. The combination of the spherical soft matrix, together with the geometry of the sensitive elements, produce sensors that are suitable for handling or robotic grasping. Indeed, the spherical shape gives an increased contact area at

greater forces, maintaining low pressure, and enabling fragile objects to be suitably handled. Furthermore, the position of the sensitive element enables the simultaneous assessment of normal and tangential forces that occur during this process. This is demonstrated in this work through the development of a simple shear sensor mounted in a gripper device able to handle an object using as a feedback control the compression and the shear forces provided by a two quadrants hemispherical sensor. Diode type sensors, linear response and combined, normal and shear forces, are suitable choices for a wide variety of applications, for example, these sensors can be specially designed to respond at a specific value of indentation or deformation. This strategy may prove useful in the control of biomechanical devices. Table 1 summarizes the main characteristics of the different sensors developed along this study and allows to compare them.

Finally, the accuracy of the numerical methodology used in this study to estimate changes in both the cross section and elongation along a channel could be improved. The methodology is more accurate when the conductive elements are positioned so the channels follow the geometry of the principal axis of stress. This is since the gel used to fabricate the conductive elements cannot be subjected to significant shear stress at the channel's boundaries. Furthermore, in practice, locating channels along the principal axis gives a monotonic sensor response.

[Table 1 about here.]

### Acknowledgements

F.M. acknowledges ANID-Chile for financial support through projects N° 1201013 and Fondecup N° 130149. Support from LIA-MSD France-Chile (Laboratoire International Associé CNRS, "Matière: Structure et Dynamique") is greatly acknowledged. We acknowledge the support from DICYT Grant 041931MH-POSTDOC of Universidad de Santiago de Chile. A.I. acknowledges the support from Conicyt National Doctorate Scholarship N° 21170673. B.D.T. was supported for this work by ANR PIA funding: ANR-20-IDEES-0002.

### References

- <sup>1</sup> Y. Roudaut, A. Lonigro, B. Coste, et al. "Touch sense," *Channels*, 2012.
- <sup>2</sup> D. M. Vogt, Y. L. Park, and R. J. Wood, "Design and characterization of a soft multi-axis force sensor using embedded microfluidic channels," *IEEE SENSORS JOURNAL*, 2013.
- <sup>3</sup> S. J. Woo, J. H. Kong, D. G. Kimb, et al. "A thin all-elastomeric capacitive pressure sensor array based on micro-contact printed elastic conductors," *J. Mater. Chem. C*, 2014, 2014.
- <sup>4</sup> S. H. Yoon, K. H. Yunbo, Z. G. Chen, et al. "isoft: A customizable soft sensor with real-time continuous contact and stretching sensing," *UIST '17 2017*, 2017.
- <sup>5</sup> H. Cho, H. Lee, Y. Kim, et al. "Design of an optical soft sensor for measuring fingertip force and contact recognition," *Int. J. Control Autom. Syst.* 15, 2017.
- <sup>6</sup> S. Kim, D. Jeong, J. Oh, W. Park, et al. "A novel all-in-one manufacturing process for a soft sensor system and its application to a soft sensing glove," in *2018 IEEE/RSJ International Conference on Intelligent Robots and Systems (IROS)*, pp. 7004–7009, 2018.
- <sup>7</sup> D. Ma, S. Ceron, G. Kaiser, et al. "Simple, low-cost fabrication of soft sensors for shape reconstruction," *IEEE Robotics and Automation Letters*, vol. 5, no. 3, pp. 4049–4054, 2020.
- <sup>8</sup> A. Grosskopf, R. Truby, H. Kim, et al. and H. A. Stone, "Viscoplastic matrix materials for embedded 3d printing," *ACS Appl. Mater. Interfaces*, 2018.
- <sup>9</sup> A. Llamosi, and S. Toussaint, "Measuring force intensity and direction with a spatially resolved soft sensor for biomechanics and robotic haptic capability" *Soft Robotics*, 2019.
- <sup>10</sup> L. Landau and E. Lifshitz, *Course of theoretical physics: theory of elasticity*. Butterworth-Heinemann, 1986.
- <sup>11</sup> R. L. Truby, M. Wehner, A. K. Grosskopf, et al. "Soft somatosensitive actuators via embedded 3d printing," *Advanced Healthcare Materials*, 2019.

- <sup>12</sup> W. Wu, A. DeConinck, and J. A. Lewis, “Omnidirectional printing of 3d microvascular networks,” *Advanced Healthcare Materials*, 2011.
- <sup>13</sup> J. Tapia, E. Knoop, M. Mutný, et al. “Make-sense: Automated sensor design for proprioceptive soft robots,” *Soft Robotics*, 2020.
- <sup>14</sup> M. Kalantari, M. Ramezanifard, et al. “Design, fabrication, and testing of a piezoresistive hardness sensor in minimally invasive surgery,” in *2010 IEEE Haptics Symposium*, pp. 431–437, 2010.

## List of Figures

- 1 Schematic of the 3D printing technique. There are three micro controlled axes for nozzle motion, which facilitate the accurate injection of ink into the gel matrix. b) Size of the injected channel as a function of the expected diameter,  $D_s$ , for a fixed nozzle diameter ( $D = 0.5\text{mm}$ ) marked with the vertical dashed line and nozzle speed. Solid red line indicates the prediction obtained from the rate of the deposited volume. . . . . 11
- 2 The bending sensor. a) Diagram of the sensitive elements within the elastomeric matrix. b) Beam deflections, from numeric calculations, indicate the deflection occurring during experiments. Yellow points show the position of the markers used to monitor beam displacement during the experiment. c) Relative resistance variation as a function of shear strain. . . . . 12
- 3 Diagram of experimental setup, showing the contact detector of  $R_s = 15\text{mm}$ . b) Semi-circumferential sensitive element positioned at  $R = 13\text{ mm}$ . c) Sinusoidal sensitive element, positioned  $R = 13\text{mm}$  from the hemispherical center. d) Multiple semi-circumferential centered elements with different radii ( $R_1 = 14\text{mm}$ ,  $R_2 = 12\text{ mm}$ ). e) Picture of a sinusoidal sensor of 13 mm radius. . . . . 13
- 4 a) Force as a function of the indentation depth, for both the circumferential and the sinusoidal sensors.  $R_s = 15\text{ mm}$ . Orange circles depict the observed experimental force and the blue line is the predicted force from the numerical simulation. b) The relative change in resistance for the semi-circumference and the sinusoidal sensors. Circles are the experimental values, lines the numeric predictions. c) Multiple semi-circumferential elements of radii,  $R_1 = 14\text{ mm}$ ,  $R_2 = 12\text{ mm}$ . (Parameters for the numeric are:  $\mu = 0.074\text{ MPa}$  and  $\kappa_0 = 0.1653\text{ MPa}$ ). . . . . 14
- 5 Local resistance change,  $r - r_0$ , normalized to the resistivity  $\rho$  of the sensitive element of the circumferential sensor as a function of the angular position, over several indentation depths. The central region of increased resistance is associated with a reduction in the cross section of the sensitive element, due to compression. This region grows with indentation depth. Inset: the width,  $a$ , of the positive resistance zone is  $a = \sqrt{bd}$  with  $b = 1.66\text{ mm}$ . Data obtained for  $R_{in} = 13.5\text{ mm}$  and  $R_s = 15\text{ mm}$ . . . . . 15
- 6 Calculations of contact sensor resistance (Silicone Ecoflex), with a semi-spherical shape of  $R_s = 15\text{mm}$ , under vertical indentation. a) Triangular circuit, with a constant  $h = 13\text{mm}$ , and a variable triangular base,  $b$ . Linearity and sensitivity are increased with decreasing  $b$ . b) Rectangular circuit, with constant  $b$ , and variable height,  $h$ . Both linearity and sensitivity increase with increasing  $h$ . . . . . 16
- 7 Sensitivity of the resistance response,  $\partial R$  with respect to the indentation variation  $\partial d$ , as a function of frequency, for different indentation levels,  $d_s$ . . . . . 17
- 8 a) Displacement field at the vertical symmetry plane of a 15 mm radius hemispherical sensor, compressed vertically at the top by a flat surface, a distance of 2.5 mm. Color scale represents the norm of the displacement field. The indentation, the shearing and the sliding stages are illustrated. b) Force on the rigid object for the indentation and shear stage. The vertical force is blue and the friction force in the horizontal direction is orange. The horizontal axis represents both variables,  $\tilde{u}_z$  and  $\tilde{u}_y$ , the displacement of the rigid object and its horizontal movement, respectively. c) Geometry of the proposed shear sensor, composed of a circuit of two semicircles of  $90^\circ$  and 13.5 mm radius, separated at the lower end by a distance of 4 mm and joined at the top. d) Calculated electrical response for both the indentation and the shear stages are shown. The blue segmented line is  $\tilde{u}_y > 0$  and the orange line is  $\tilde{u}_y < 0$ . . . . . 18

- 9 a) Picture of the two quadrants sensor for the detection of the axial compression and the shear along a single axis. b) Configuration schematizing the cycle employed to illustrate sensor functioning: i) compression, ii) positive shear, iii) negative shear, iv) compression released. c) Direct readings,  $R_+$  and  $R_-$  of right and left quadrants, and the calculated compression and shear,  $C$  and  $S$  respectively, for the process described in b). d) Sensor is installed in one of the arms of a gripper. . . . . 19

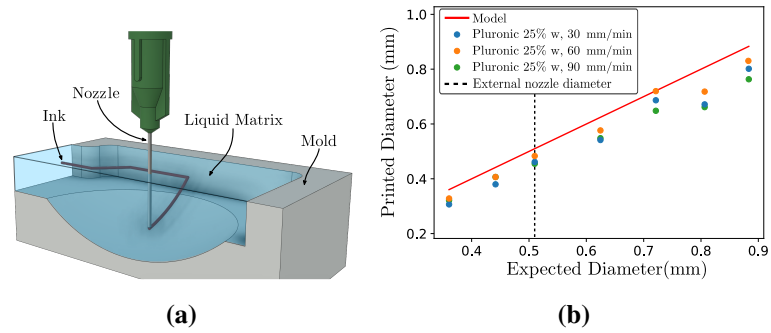


**Figure 1.** Schematic of the 3D printing technique. There are three micro controlled axes for nozzle motion, which facilitate the accurate injection of ink into the gel matrix. b) Size of the injected channel as a function of the expected diameter,  $D_s$ , for a fixed nozzle diameter ( $D = 0.5\text{mm}$ ) marked with the vertical dashed line and nozzle speed. Solid red line indicates the prediction obtained from the rate of the deposited volume.

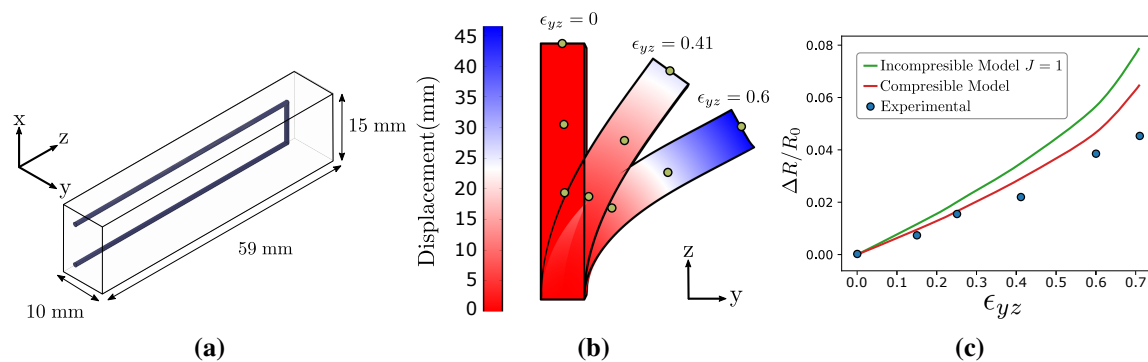


**Figure 2.** The bending sensor. a) Diagram of the sensitive elements within the elastomeric matrix. b) Beam deflections, from numeric calculations, indicate the deflection occurring during experiments. Yellow points show the position of the markers used to monitor beam displacement during the experiment. c) Relative resistance variation as a function of shear strain.

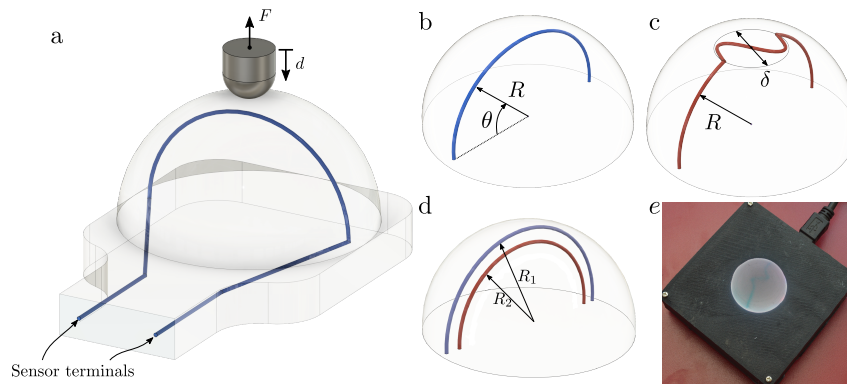


**Figure 3.** Diagram of experimental setup, showing the contact detector of  $R_s = 15\text{mm}$ . b) Semi-circumferential sensitive element positioned at  $R = 13\text{ mm}$ . c) Sinusoidal sensitive element, positioned  $R = 13\text{mm}$  from the hemispherical center. d) Multiple semi-circumferential centered elements with different radii ( $R_1 = 14\text{mm}$ ,  $R_2 = 12\text{ mm}$ ). e) Picture of a sinusoidal sensor of 13 mm radius.

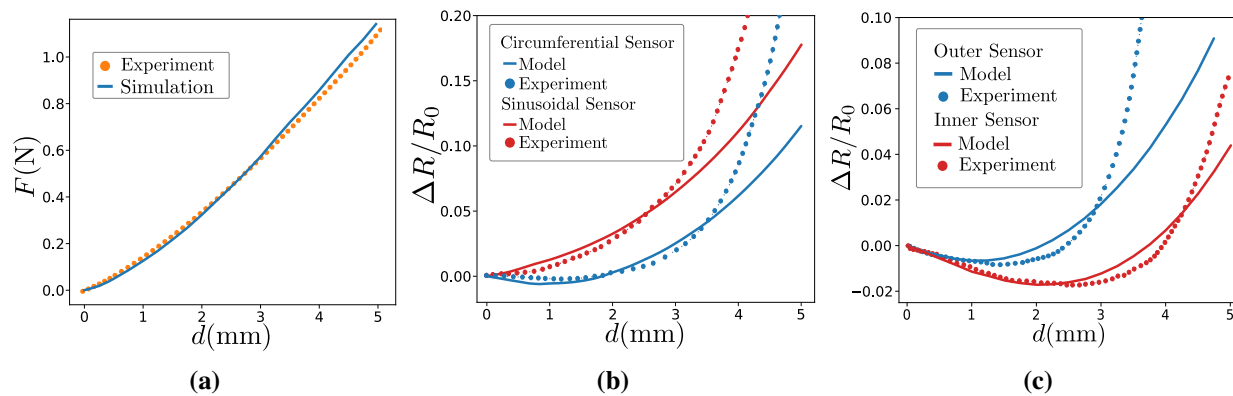


**Figure 4.** a) Force as a function of the indentation depth, for both the circumferential and the sinusoidal sensors.  $R_s = 15$  mm. Orange circles depict the observed experimental force and the blue line is the predicted force from the numerical simulation. b) The relative change in resistance for the semi-circumference and the sinusoidal sensors. Circles are the experimental values, lines the numeric predictions. c) Multiple semi-circumferential elements of radii,  $R_1 = 14$  mm,  $R_2 = 12$  mm. (Parameters for the numeric are:  $\mu = 0.074$  MPa and  $\kappa_0 = 0.1653$  MPa).

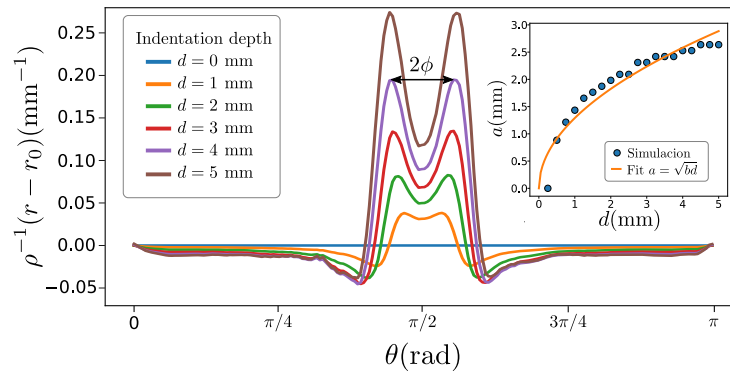
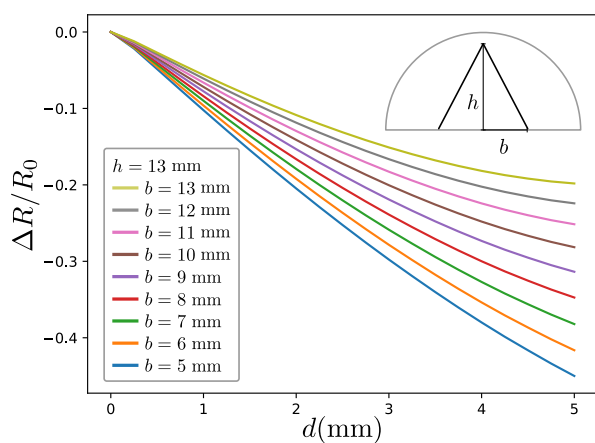
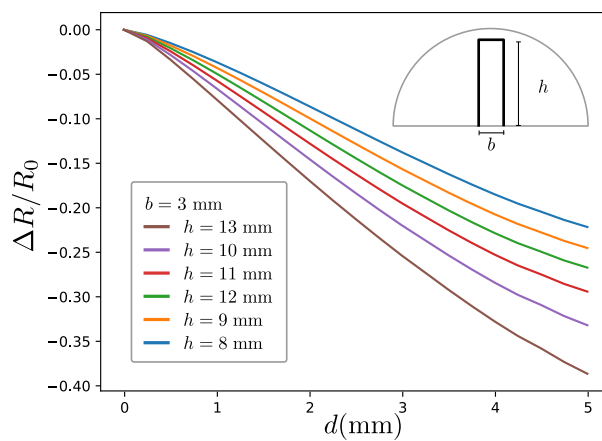


**Figure 5.** Local resistance change,  $r - r_0$ , normalized to the resistivity  $\rho$  of the sensitive element of the circumferential sensor as a function of the angular position, over several indentation depths. The central region of increased resistance is associated with a reduction in the cross section of the sensitive element, due to compression. This region grows with indentation depth. Inset: the width,  $a$ , of the positive resistance zone is  $a = \sqrt{bd}$  with  $b = 1.66$  mm. Data obtained for  $R_{in} = 13.5$  mm and  $R_s = 15$  mm.



(a) Triangular sensor.



(b) Step shape sensor

**Figure 6.** Calculations of contact sensor resistance (Silicone Ecoflex), with a semi-spherical shape of  $R_s = 15$  mm, under vertical indentation. a) Triangular circuit, with a constant  $h = 13$  mm, and a variable triangular base,  $b$ . Linearity and sensitivity are increased with decreasing  $b$ . b) Rectangular circuit, with constant  $b$ , and variable height,  $h$ . Both linearity and sensitivity increase with increasing  $h$ .

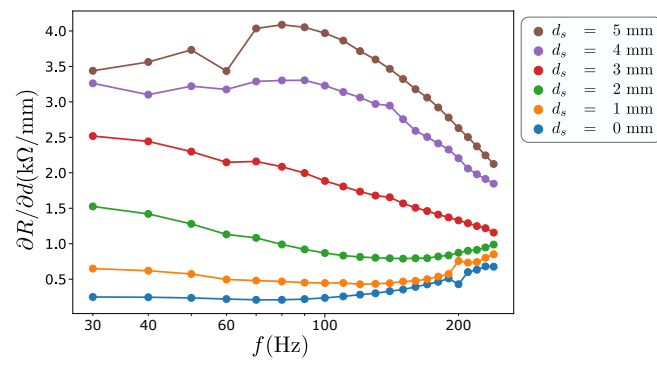


**Figure 7.** Sensitivity of the resistance response,  $\partial R$  with respect to the indentation variation  $\partial d$ , as a function of frequency, for different indentation levels,  $d_s$ .

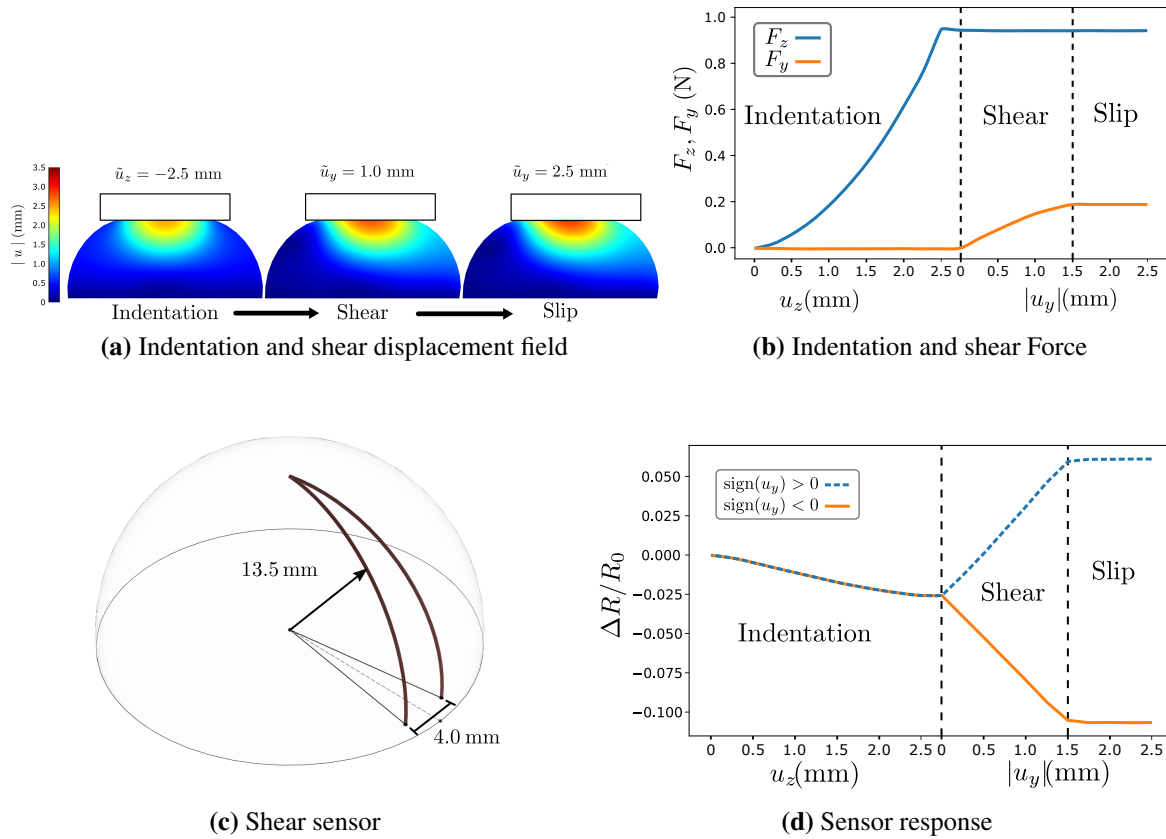


**Figure 8.** a) Displacement field at the vertical symmetry plane of a 15 mm radius hemispherical sensor, compressed vertically at the top by a flat surface, a distance of 2.5 mm. Color scale represents the norm of the displacement field. The indentation, the shearing and the sliding stages are illustrated. b) Force on the rigid object for the indentation and shear stage. The vertical force is blue and the friction force in the horizontal direction is orange. The horizontal axis represents both variables,  $\tilde{u}_z$  and  $\tilde{u}_y$ , the displacement of the rigid object and its horizontal movement, respectively. c) Geometry of the proposed shear sensor, composed of a circuit of two semicircles of  $90^\circ$  and 13.5 mm radius, separated at the lower end by a distance of 4 mm and joined at the top. d) Calculated electrical response for both the indentation and the shear stages are shown. The blue segmented line is  $\tilde{u}_y > 0$  and the orange line is  $\tilde{u}_y < 0$ .

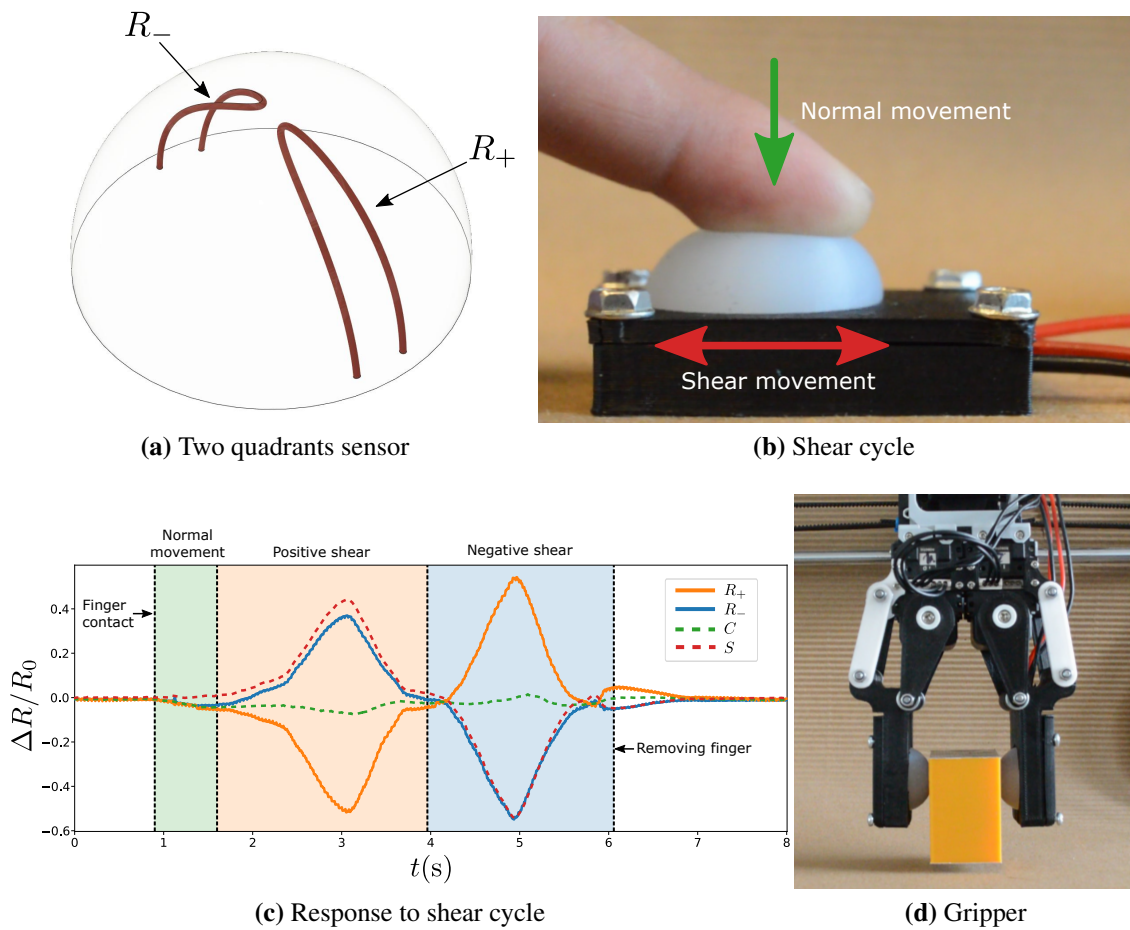


**Figure 9.** a) Picture of the two quadrants sensor for the detection of the axial compression and the shear along a single axis. b) Configuration schematizing the cycle employed to illustrate sensor functioning: i) compression, ii) positive shear, iii) negative shear, iv) compression released. c) Direct readings,  $R_+$  and  $R_-$  of right and left quadrants, and the calculated compression and shear,  $C$  and  $S$  respectively, for the process described in b). d) Sensor is installed in one of the arms of a gripper.

**List of Tables**

1 Summary of sensor characteristics . . . . . 21

Sensors	Advantages	Disadvantages
Rectangular beam	quasi-linear response with shear strain	low sensitivity
Cap with semi-circumference circuit	threshold response to indentation	non-monotonic response
Cap with sinusoidal circuit	monotonic response and high sensitivity	-
Cap with multiple semi-circumferencial circuit	threshold response with selecteable onset	non-monotonic response
Cap with radial circuit	enhanced sensitivity to axial compression	linear response
Cap with with two semi-arches circuits	sensitive to both compression and shear; good linearity	low sensitivity to compression as compared to shear

Table 1. Summary of sensor characteristics